Chemical Engineering Journal 482 (2024) 148937

Contents lists available at ScienceDirect

Chemical Engineering Journal

journal homepage: www.elsevier.com/locate/cej

Photo-triggered multifunctional gold-based hybrid nanoflowers promote infectious skin regeneration

Jixuan Hong [a,1], Jiaqi Zhu [a,1], Xiaxin Cao [a], Boqi Pang [a], Jiaru Xian [a], Xueqiong Yin [a], Qiaoyuan Deng [a,b,*], Maohua Chen [a], Ziyu Qin [a], Chaozong Liu [c], Swastina Nath Varma [c], Yin Xiao [d], Lan Xiao [d,*], Mengting Li [a,*]

[a] *Hainan Provincial Fine Chemical Engineering Research Center, School of Chemical Engineering and Technology Hainan University Haikou, Hainan 570228, P. R. China*
[b] *Key Laboratory of Advanced Material of Tropical Island Resources of Educational Ministry School of Materials Science and Engineering Hainan University Haikou, Hainan 570228, China*
[c] *Institute of Orthopaedic & Musculoskeletal Science, University College London, Royal National Orthopaedic Hospital, London HA7 4LP, UK*
[d] *School of Medicine and Dentistry, Griffith University (GU), Gold Coast, QLD 4222, Australia*

ARTICLE INFO

Keywords:
Mild photothermal antibacterial therapy
Gold-based hybrid nanoflowers
Photo-triggered drug release
Anti-inflammation
Infectious skin tissue regeneration

ABSTRACT

The skin wound-healing under infectious conditions remains challenging owing to the lack of efficient strategies to inhibit drug-resistant bacteria growth and control inflammation. Photothermal therapy shows efficient antimicrobial effects, whereas it generates excessive heat to damage tissue and inflammation to impair tissue regeneration. Herein, we develop the multifunctional gold-based nanoflowers incorporated with photosensitizer (Ce6, for PDT) and anti-inflammatory drug (bromfenac sodium/BS). This allows for a nanosystem to combine the mild-photothermal therapy (mPTT), photodynamic therapy (PDT), and drug-controlled release anti-inflammation therapy for infectious skin regeneration. Upon laser irradiation, the local temperature increased (to a mild temperature of ~ 45 ℃, mPTT) along with the singly linear oxygen (from PDT) for anti-infection; the release of BS was triggered for anti-inflammation. The multifunctional nanoflowers achieved 99 % antibacterial efficiencies and biofilm inhibition *in vitro*. They showed good biocompatibility and improved wound-healing in the animal models of subcutaneous abscess and skin wound infected with drug-resistant bacteria. In addition to the antibacterial effect from mPTT and PDT, the nanoflowers regulated the immune microenvironment by controlled releasing BS, inhibiting inflammation and promoting growth factor production, collagen deposition, and angiogenesis to improve skin wound-healing. Therefore, this study provides an advanced nano-system with photo-triggered antimicrobial and anti-inflammation activities, which improves infectious skin tissue regeneration.

1. Introduction

Despite recent advances in antimicrobial techniques and materials, bacterial infection remains a clinical challenge [1–3]. Infected skin issues will exhibit redness and swelling, elevated skin temperature, a certain amount of pain, and even more severe symptoms such as painful involuntary movements and metabolic and immune system disorders [4,5]. The healing of infectious skin wounds could be problematic due to the host immune responses to bacterial infection, which can induce chronic inflammation along with the excessive production of inflammatory cytokines, contributing to an unfavorable microenvironment for angiogenesis and collagen deposition and thereby impairing wound-healing [6,7]. Therefore, there is an urgent need for advanced approaches with antibacterial and anti-inflammatory effects to synergistically promote infectious skin regeneration.

The traditional anti-infection approaches, including antibiotics and inorganic antimicrobial agents, may cause microbial resistance and serious systemic toxicity [8–10]. To address these issues, a variety of

---

[*] Corresponding authors at: Key Laboratory of Advanced Material of Tropical Island Resources of Educational Ministry School of Materials Science and Engineering Hainan University Haikou, Hainan 570228, China (Q. Deng). G40 Room 7.61, Griffith University Gold Coast Campus, QLD 4222, Australia (L. Xiao). Hainan Provincial Fine Chemical Engineering Research Center, School of Chemical Engineering and Technology Hainan University Haikou, Hainan 570228, P. R. China (M. Li).

E-mail addresses: qydeng@hainanu.edu.cn (Q. Deng), l.xiao@griffith.edu.au (L. Xiao), limengting@hainanu.edu.cn (M. Li).

[1] Those authors contribute equally to the manuscript and are co-first authors.

https://doi.org/10.1016/j.cej.2024.148937
Received 7 December 2023; Received in revised form 14 January 2024; Accepted 18 January 2024

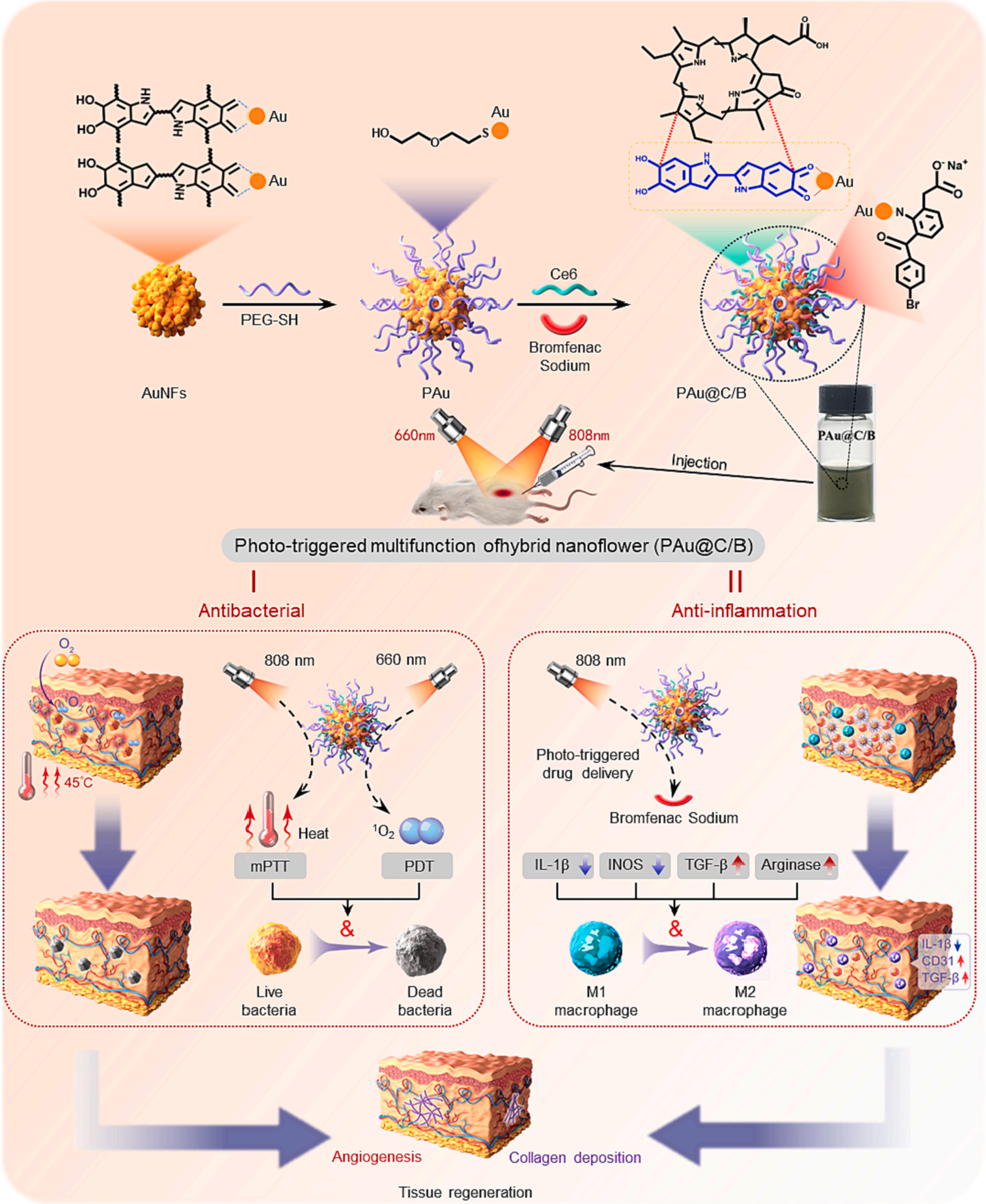

Scheme 1. The synthesis and multifunction of PAu@C/B in promoting infectious skin tissue regeneration.

precise treatment approaches for bacterial infections have been developed, such as radiation therapy, photothermal therapy (PTT), photodynamic therapy (PDT), gas therapy [11], etc. PTT utilizes nanomaterial-based photothermal agents (PTAs) to convert the absorbed photon energy into heat to kill bacteria. PTT has shown advantages such as minimal invasiveness, high selectivity, and negligible drug resistance [12]. Among the nanomaterial candidates for PTT, gold nanoparticles (AuNPs) have received widespread attention due to their excellent photothermal properties and biosafety [13,14].

The antibacterial effect of PTT is positively correlated with the photothermal temperature. For efficient anti-infection, the temperature required for PTT is ~ 50 °C and can damage healthy tissue [15–17]. To solve this problem, a combination of mild-temperature thermotherapy (~45 °C) and PDT is preferred in infectious skin tissue healing. The mechanism of PDT is based on the photochemical reactions of photosensitizers (PSs). Upon irradiation using a laser with a wavelength matching the absorption of the PSs, reactive oxygen species (ROS, such as hydroxy radicals, superoxides, or singlet oxygen($^1O_2$)) are generated to damage bacterial membranes and DNA molecules [18]. A combination of PTT and PDT can synergistically reduce bacterial growth and avoid tissue damage from the high temperature thermotherapy [19–22].

On the other hand, both PTT and PDT can cause tissue inflammation, an unfavorable wound-healing microenvironment owing to the activation of immune cells such as M1 (inflammatory) phenotype macrophage [23,24]. Factors from the inflammatory environment in the infected wound such as interleukin-1β (IL-1β) and ROS can induce excessive fibrosis and oxidative stress to hinder wound healing [25]. On the other hand, anti-inflammatory drug such as bromfenac sodium (BS) can covert the inflammatory environment into the one providing tissue regeneration factors (e.g., tissue growth factor-β (TGF-β)) to improve wound healing [26,27]. This is because anti-inflammatory drug can induce the phenotype switch in immune cells from their inflammatory phenotype (e.g., M1 macrophage) to anti-inflammatory phenotype (M2 macrophage) to favor mesenchymal progenitor cell recruitment and angiogenesis [28], a immunomodulatory strategy with demonstrated positive effects in tissue regeneration [29,30]. Therefore, it is crucial to endow the photothermal nanomaterials with anti-inflammatory capacity to generate an environment benefiting tissue regeneration.

Due to its versatility in size and shape, AuNPs are also frequently used as carriers for controlled release of drugs for anti-inflammation [31]. The use of dopamine as surface ligands, for example, has allowed the development of carriers to deliver drugs to specific locations [32–36], suggesting the rationale to use polydopamine-modified AuNPs to deliver both photosensitizer and anti-inflammatory factors, therefore, ensure a combined mPTT-PDT therapy along with immunomodulation for infectious wound-healing. However, the traditional synthesized AuNPs with polydopamine modification have a wide size distribution, and their aggregation in liquids limits their applications [37]. This suggests that more advanced gold-based nanomaterials are required.

In our recent finding, a type of polydopamine-gold composite nanoflowers (AuNFs) has been developed via the template approach [38], which has shown advantages over the traditional AuNPs, such as significantly improved dispersion and high photothermal conversion. Therefore, in the current study, AuNFs were adopted for mPTT, with the incorporation of PS chlorin e6 (ce6, for PDT) and BS (for anti-inflammation) to obtain a multifunctional hybrid nanoflower system (photothermal ce6-BS loading gold nanoflowers, PAu@C/B). We demonstrated that in response to laser irradiation, this nanosystem can induce the photothermal and photodynamic antimicrobial effects (against Staphylococcus aureus (*S. aureus*) and Escherichia coli (*E. coli*)) and release BS to regulate the inflammatory microenvironment. These synergistic effects eventually led to a favorable microenvironment for collagen deposition and angiogenesis, thereby significantly improving infectious skin regeneration *in vivo*. This study, therefore potentially provides an innovative nanomaterial-based therapeutic approach (PAu@C/B) for infectious wound-healing (Scheme 1).

2. Materials and methods

2.1. Materials

Bacterial cellulose (BC) with a thickness of 2.0 mm was provided by Hainan Yida Food Co., Ltd. (Hainan, China). Dopamine hydrochloride was obtained from Sigma Aldrich (St Louis, MO, USA). α-methoxy–mercaptopolyethylene glycol (mPEG-SH, 5000 MW) was obtained from Sinopharm Chemical Reagent CO.,Ltd. (China). Chlorine e6 (Ce6) and Bromfenac sodium (BS) were purchased from Frontier Scientific. The other chemicals and reagents were analytical grade and were used as received without further purification. *E. coli* (ATCC 25922), *S. aureus* (ATCC 6538), *MRSA* and mouse L929 fibroblasts that were used in this study were obtained from the Haikou People's Hospital (Hainan, China). An individual colony was separated from the LB agar plate and added to fresh LB broth, and then shaken at 220 rpm overnight at 37 °C. Diluted the overnight bacterial solution 1:100 and shook for another 2 h to make sure the bacteria were in log growth phase before the experiment.

2.2. Preparation of PAu@C/B

AuNFs were synthesized via templated method as previously described [39]. In brief, BC sheets were immersed in 2 mg/mL dopamine hydrochloride in 10 mM (pH 8.5) Tris-buffer for polydopamine (PDA) deposition (BC/PDA) for 24 h. Then, the obtained BC/PDA sample was immersed in $HAuCl_4$ solution (0.01 wt%) for 9 h for gold particle development, followed by vibration with ultrasound, washing with deionized water, and centrifugation to collect the AuNFs. And then, AuNFs (1 mg/mL) were suspended in mPEG-SH (1 mg/mL) solution for 24 h to obtain PEG-AuNFs (PAu). Finally, PAu@C/B was prepared by mixing of PAu (1 mg/mL) suspension with a solution containing Ce6 (1 mg/mL) and BS (1 mg/mL) for 24 h, followed by centrifugation to remove the free drugs. The precipitate was collected and the content of unloaded drugs was determined by UV–vis spectroscopy. The drug loading content (DLC) was calculated according to the following formula:

$$DLC\ (wt\%) = \frac{The\ weight\ of\ loaded\ drug\ (Ce6\ or\ BS)}{The\ weight\ of\ PAu@B/C} \times 100\%$$

2.3. Nanomaterial physicochemical characterizations

The microstructures of the prepared AuNFs, PAu and PAu@C/B, were observed by scanning electron microscopy (SU8020, HITACHI, Japan) and transmission electron microscopy (FEI Tecnai F20). UV–vis–NIR absorption spectra were obtained using a TU-1901 spectrophotometer (China). The contents of Au in AuNFs, PAu and PAu@C/B were determined by inductively coupled plasma-mass spectrometry (ICP-MS) (Thermo Electron). The hydrodynamic size and zeta potential of AuNFs, PAu and PAu@C/B were measured by the Malvern zetasizer (ZS90, Malvern, UK).

2.4. Photothermal performance assay

The photothermal capacities of AuNFs, PAu and PAu@C/B were detected by an infrared thermometer (LR-MFJ-808, Ningbo, China). Different sample dispersions (200 μg/mL) were irradiated under 808 nm NIR (1.5 W/cm^2). At the designated time points, the corresponding temperature was recorded using a thermal camera (Testo 871). Moreover, the temperature variations were recorded for a total of five thermal/cooling cycles of laser on/off to evaluate the photothermal stability.

2.5. Photodynamic performance assay

DPBF was used as an indicator to detect $^1O_2$. Briefly, 40 μL DPBF (1 mg/mL) was added into 2 mL AuNFs, PAu and PAu@C/B dispersions (200 mg/mL) respectively, followed with continuous laser irradiation (660 nm, 1 W cm^{-2}) for 10 min. UV–vis absorbances of the mixed solutions were recorded every minute. We have further employed the ESR technique to detect the photogeneration of $^1O_2$ by PAu@C/B using 2,2,6,6-tetramethyl piperidine (TEMP) as the spin trap agent.

2.6. Photo-triggered drug release assay

PAu@C/B was exposed to NIR irradiation to determine whether the mild-photothermal effect triggered drug release. The solution of PAu@C/B in PBS was irradiated with an 808 nm NIR laser and controlled the mild photothermal temperature at 45 ℃ for 10 min, followed by 30 min intervals without NIR laser irradiation. Then, the PAu@C/B solution was centrifuged (11000 rpm, 10 min) to obtain the supernatant, and the released Ce6 and BS were determined by measuring the absorbance of the supernatant using UV–vis. The released dose of them was calculated according to their standard curve, respectively. After that, the PAu@C/B solution was irradiated once more, and the absorbance of the supernatant was recorded as well. This "on" and “off” process was repeated three times. Furthermore, the NIR-promoted drug release was further investigated by irradiating PAu@C/B once at a mild temperature of 45 °C. At selected time points, the PAu@C/B solution was centrifuged, and the UV–vis absorption of the supernatant was determined. The released dose of Ce6 and BS was calculated using the respective standard curves.

2.7. In vitro antibacterial assay

To evaluate the antibacterial activities of PAu@C/B under laser irradiation, Gram-negative bacteria Escherichia coli (*E. coli*) and Gram-positive bacteria (*S. aureus)* were selected as model microbes. The number of bacteria was determined using the spread plate assay. Briefly, 1×10^6 CFU/mL bacteria were cultured with PAu@C/B in 96-well plates for 30 min. Then, the mixtures were subjected to 808 nm (45 ℃ for 10 min) or /and 660 nm (300 mW/cm^2 for 10 min) laser irradiation. After dilution to a suitable concentration with PBS, 70 μL the bacterial suspension was plated on LB agar to incubate at 37 ℃ for 12 h. The antibacterial rate of PAu@C/B for different therapies was evaluated by counting the number of bacterial colony-forming units (CFUs) using the following formula: $A = (B - C)/B \times 100\ \%$, where A indicates the antibacterial ratio; B is the average CFU of the control (PBS), and C is the average CFU of other four groups: PAu@C/B, PAu@C/B + mPTT, PAu@C/B + PDT, PAu@C/B + mPTT + PDT (mPTT indicates under 808 nm NIR laser, PDT indicates under 660 nm NIR laser). All the experiments were performed in triplicate. Furthermore, the morphology of bacteria (*S. aureus* and *E. coli*) with the above-mentioned different treatments was also investigated by SEM (Hitachi Su 8010) instrument at 3.0 kV. Briefly, bacteria with different treatments were fixed with 2 % glutaraldehyde at 4 °C for 4 h, dehydrated using ethanol solution gradient of 50 %, 70 %, 90 %, 95 %, and 100 % for 15 min, and then evenly spread on the silicon wafer superior. Before being observed, the samples were delicately blown-dried with nitrogen and sprayed with gold using a sputtering technique. In addition, Live/dead (green/red) staining assay was taken with a bacterial viability kit (Molecular Probes L7012) for detailed analysis, and photos were captured by a confocal microscope (CLSM, Leica TCS SP8).

2.8. In vitro antibiofilm assay

In order to test and verify the anti-biofilm effect of PAu@C/B under dual laser irradiation, bacterial suspensions were subjected to different therapies and divided into five groups as follows: PBS, PAu@C/B, PAu@C/B + mPTT, PAu@C/B + PDT, PAu@C/B + mPTT + PDT. Following that, the biofilm of *S. aureus* corresponding to the above solutions was stained with crystal violet (CV) for quantification.

2.9. In vitro cytotoxicity evaluation

The CCK-8 (Dojindo, Kumamoto, Japan) assay was used to assess the biocompatibility of the nanoflowers using L929 fibroblasts. L929 fibroblasts were seeded at a density of 2×10^4 in a 96-well plate and cultured with regular medium for 12 h. Subsequently, the medium was replaced with a condition medium containing various concentrations (25 and 50 μg/mL) of nanoflowers (AuNFs, PAu and PAu@C/B). After 24 h of culture, cell viability was measured using the CCK-8 assay. At the same time point, cell proliferation was further evaluated by live/dead staining. Briefly, L929 cells were washed thrice with PBS and then stained with acridine orange (AO, Sigma Aldrich) and propidium iodide (PI, Sigma Aldrich) solution for 10 min. Finally, the stained samples were observed under a fluorescence microscope (Leica DM50000B).

2.10. In vitro evaluation of immunomodulatory capacity

To evaluate the effect of PAu on macrophage inflammatory response, the murine macrophage cell line (RAW 264.7, RAW cells) was used. Briefly, RAW cells were cultured with Dulbecco’s modified Eagle’s medium (DMEM; Gibco TM, Thermo Fisher Scientific, Waltham, MA, USA) containing 5 % (v/v) fetal bovine serum (FBS, heat-inactivated at 60 °C for over 30 min, Lonza, Basel, Switzerland) and 1 % (v/v) penicillin/streptomycin (P/S, Gibco TM, Thermo Fisher Scientific, Waltham, MA, USA) according to previous publications [40]. The culture medium was changed every 2–3 days. Cells (when reaching 80 % confluence) were passaged by treating with 0.25 % trypsin (containing 1 mM EDTA) for 2 min.

To simulate infection-induced inflammatory conditions *in vitro*, RAW cells were stimulated with 100 ng/mL lipopolysaccharides (LPS) for 24 h. PAu at graded concentrations (0, 25, 50 μg/mL, 0 μg/ml served as the vehicle LPS control group) were used to treat cells upon LPS stimulation. After that, cells were harvested, and total RNA was isolated using the TRIzol Reagent (Ambion®, Thermo Fisher Scientific, Waltham, MA, USA) for real-time polymerase chain reaction (qPCR) as previously described [29]. 1 μg total RNA was used to synthesize cDNA using the SensiFAST™ cDNA Synthesis Kit (Bioline Reagents, Meridian Bioscience Inc., Cincinnati, OH, USA) following the manufacturer’s protocol. The qPCR was then performed to analyze the mRNA levels of the following target genes in RAW cells: *CD80, CD86, IL-1β, IL-6, TNF,* and *CD206* (sequences listed in Table S1). The housekeeping gene *Gapdh* was used as control. The relative gene expression was normalized against *Gapdh* calculated as previously described [41]. All experiments followed the MIQE guidelines [42] and were replicated for three times.

2.11. In vivo antibacterial assay

To further investigate the antibacterial effect *in vivo*, the subcutaneous abscess model and wound-healing model were developed in Kunming mice. PAu@C/B nanoflowers (concentration: 1 mg/mL, total volume: 50 μL) were locally injected and exposed to 808 nm or 660 nm irradiation. For the subcutaneous abscess model, the mice were anesthetized and injected subcutaneously with *MRSA* (100 μL, 1.0×10^9 CFU/mL) on their backs, and the model establishment was confirmed after 24 h, and an obvious abscess area was observed subcutaneously in Kunming mice, indicating that the subcutaneous abscess model was successfully created. For the wound-healing model, after removing the back hair, an 8.0 mm diameter wound was cut on the back with scissors. The wound site was infected with *MRSA* suspension (20 μL, 1.0×10^9 CFU/mL) to establish the *MRSA*-infected wound model. During the photothermal antimicrobial therapy, the NIR image was used to record the temperature changes around the abscess and wound to evaluate the *in-situ* imaging performance of PAu@C/B. The wound area of mice was calculated by Image J software.

The standard plate counting method was used to quantitatively evaluate the anti-bactericidal effects of different groups in mice. Hematoxylin and eosin (H&E) staining was used for histological analysis of skin sections to evaluate the safety of PAu@C/B during mild photothermal-photodynamic therapy (mPTT-PDT) for anti-infection and anti-inflammatory therapy via controlled drug release under dual lasers irradiation. All test groups and control groups contained five parallel groups for repeatability evaluation.

2.12. Histological, immunofluorescence, and immunohistochemistry analysis

For the subcutaneous abscess model, the animals were sacrificed on days 7 and 14 after surgery. For the wound-healing model, the animals were sacrificed on days 7 and 12 after surgery. The wound tissues of the mice were collected, fixed with 4 % paraformaldehyde, and embedded in paraffin to slice into 5 μm thick tissue sections. For day 7 and day 12/day 14 samples, hematoxylin and eosin (H&E) staining was performed for histological observation. For day 12/day 14 samples, Masson staining was performed for the detection of collagen deposition. Immunofluorescent staining was performed to evaluate the angiogenesis

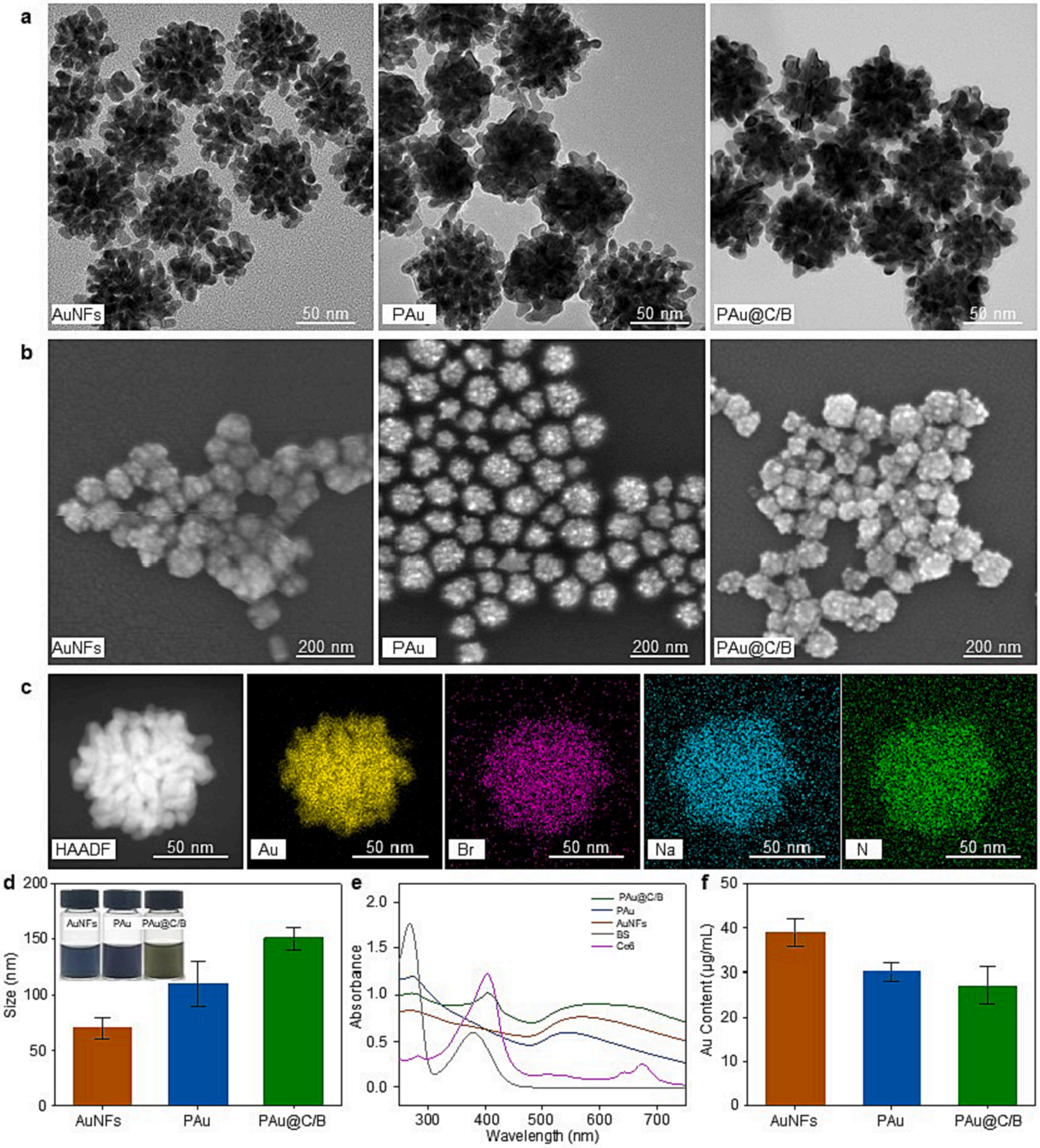

Fig. 1. Characterizations of AuNFs, PAu and PAu@C/B. (a) TEM and (b) SEM of AuNFs, PAu and PAu@C/B. (c) Element mapping images of PAu@C/B. (d) Average sizes of AuNFs, PAu and PAu@C/B. The inserts are the general images of AuNFs, PAu and PAu@C/B. (e) UV–vis spectra of AuNFs, PAu, PAu@C/B, BS and Ce6. (f) Au content in AuNFs, PAu and PAu@C/B (sample concentration at 200 μg/mL).

potential to detect the expression of CD31 (ab64543, Abcam), and the expression of IL-1β and TGF-β (n = 6), and IL-1β primary antibodies (GB11113, Servicebio) and corresponding secondary antibodies were used to determine the inflammatory and tissue regenerative factors in wound tissue, respectively. Immunohistochemical (IHC) staining was used to detect the infiltration of M1-like (iNOS$^+$, ab15323, Abcam) and M2-like (arginase$^+$, #93668, CST) cells in the wound tissue. Image J software was used for the quantification of positive stains.

2.13. *Statistical analysis*

All quantitative data were analyzed using one-way ANOVA and expressed as mean values ± standard deviations. The student's *t*-test was used to evaluate the statistical significance of variance. Values of $^*p < 0.05$ were considered statistically significant.

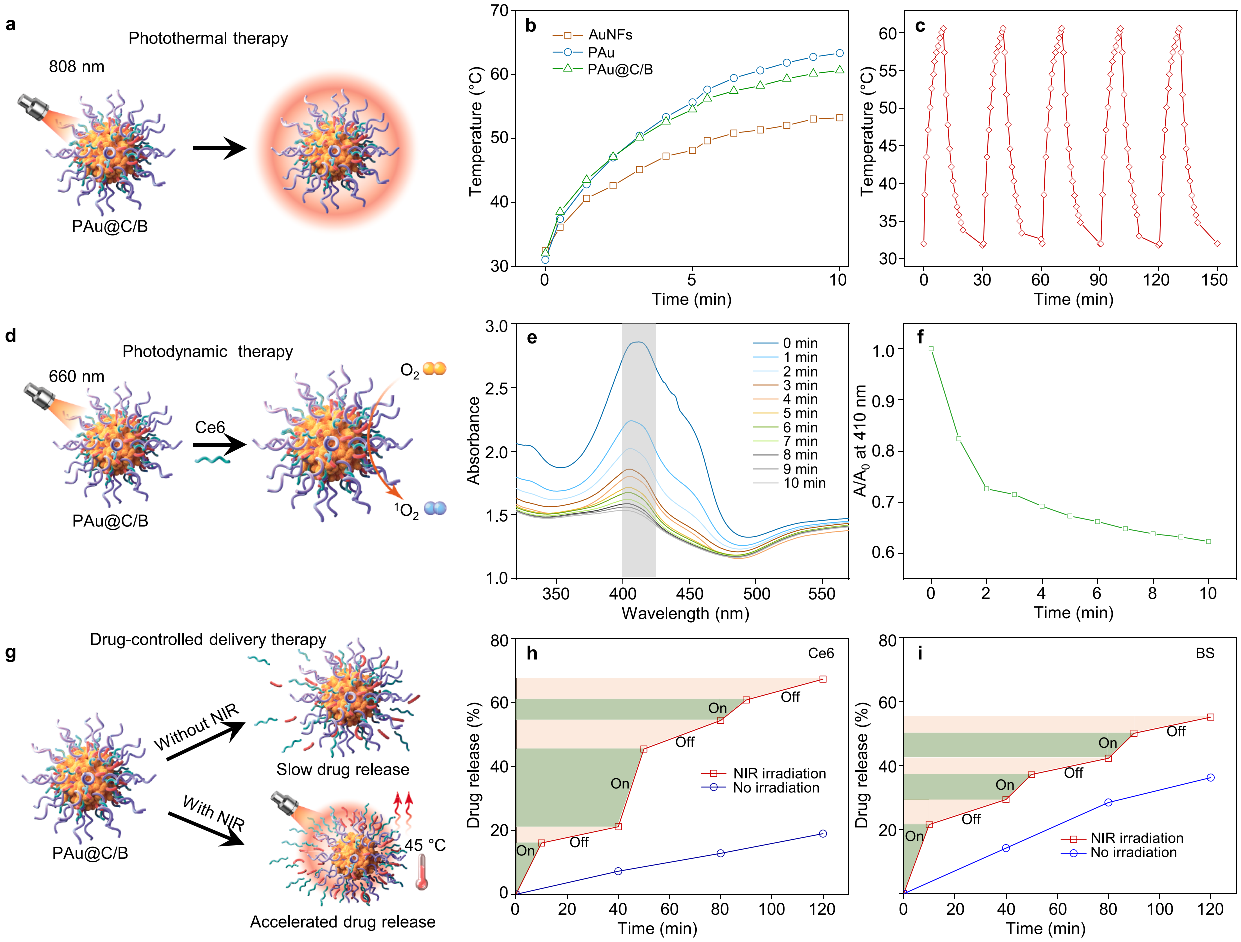

Fig. 2. Multifunctionality of PAu@C/B. (a) Photothermal effects of PAu@C/B. (b) Temperature increases of AuNFs, PAu and PAu@C/B with time upon the irradiation at 808 nm and 1.5 W/cm^2. (c) The temperature profile of PAu@C/B during five on/off cycles of NIR laser irradiation. (d) Photodynamic effect of PAu@C/B. (e) UV–vis spectra changes of DPBF + PAu@C/B with time upon the irradiation at 660 nm and 1 W/cm^2, and (f) the corresponding changing curve of PAu@C/B. (g) NIR-triggered drug release from PAu@C/B. (h) Mild-photothermal temperature (45 °C) triggered Ce6 release. (i) Mild-photothermal temperature (45 °C) triggered BS release.

3. Result and discussion

3.1. Preparation and characterization of PAu@C/B

The PAu@C/B synthesis procedure and the typical structures and properties of PAu@C/B are presented in Fig. 1. In these drug-loaded hybrid nanoflowers, AuNFs were synthesized by a template technique [43]. Mecaptoated PEG was then self-assembled to improve the biocompatibility and hydrophilicity of AuNFs. Dual drugs Ce6 (PS) and BS (an anti-inflammatory drug) were facilely adsorbed onto the hybrid nanoflowers to finally form PAu@C/B. The as-prepared PAu@C/B showed a dandelion-like morphology with a diameter of about 70 nm (Fig. 1a and b). This indicates the self-assembly of PEG and the further integration of Ce6 and BS have little effect on the size and morphology of the hybrid nanoflowers. However, compared to AuNFs, the average hydrodynamic diameter of PAu@C/B (measured by DLS) increased from 108 ± 15.1 nm to 141 ± 10.1 nm (Fig. 1d). This diameter increase is mainly attributed to the PEG chains, which extend the hydration layer on the nanoflower surfaces. This study used dopamine for the preparation of Au-based nanoflowers. As a result, the elemental mapping analysis (Fig. S1) indicates that PAu and AuNFs nanoflowers contain N, C, O, and Au elements. Furthermore, PAu@C/B were prepared by mixing PAu nanoflowers with a Ce6 and BS solution. This allowed the dual drugs to adsorb onto the surface of hybrid nanoflowers. Therefore, Br and Na elements can also be detected in PAu@C/B sample (Fig. 1e). In addition, these PAu@C/B hybrid nanoflowers exhibited a net negative charge around −15.4 mV (zeta potential in Fig. S2), which can facilitate the accumulation of nanoflowers in the inflammatory tissues [44,45].

The UV–vis absorbance of PAu@C/B, AuNFs, PAu, Ce6 and BS were compared (Fig. 1e). The characteristic peak redshifts from 520 nm for PAu to 560 nm for PAu@C/B. This broadening could be due to the presence of PEG, which decreased the dielectric constant/polarity of the medium and altered the solution parameters. Besides, PAu@C/B exhibited an obviously enhanced absorption at 404 nm and 269 nm, corresponding to the incorporation of Ce6 and BS, respectively. The loaded Ce6 also endowed PAu@C/B with stronger fluorescence than AuNFs and PAu (Fig. S3). The loading contents of Ce6 and BS were approximately 26.6 wt% and 21.9 wt%, respectively (Fig. S4). On the other hand, as a result of PEG grafting and drug loading, the Au content determined by ICP-MS in AuNFs, PAu, and PAu@C/B gradually decreased from 77.70 μg/mL to 70.19 μg/mL and then to 54.26 μg/mL (Fig. 1f).

3.2. Multifunctionality of PAu@C/B

3.2.1. Photothermal effect of PAu@C/B

Previous studies indicate that AuNFs exhibit a high photothermal efficiency (34.9 %) for light-to-heat conversion, attributing to a highly branched flower structure and a hybrid system composed of both PDA

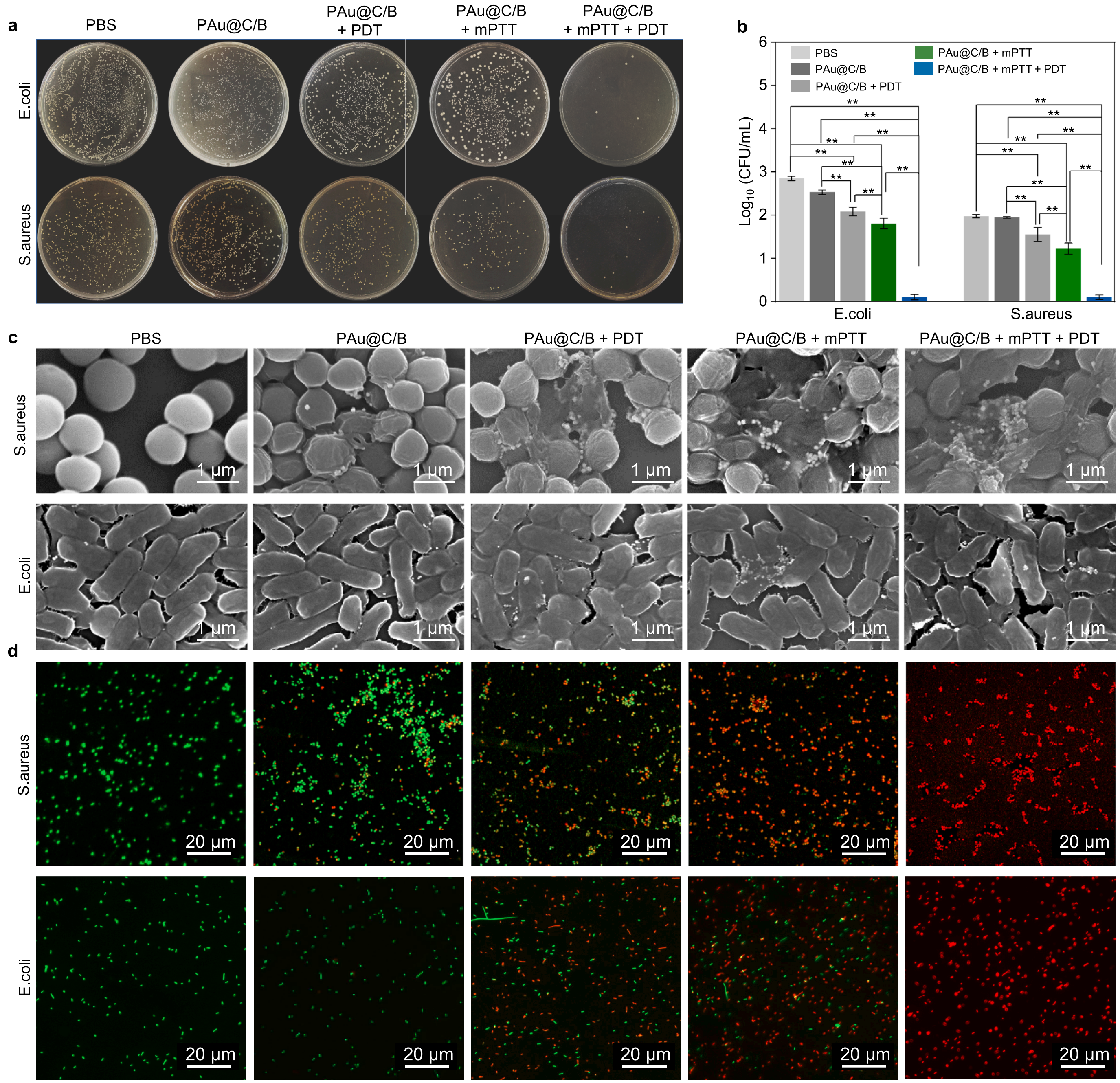

Fig. 3. *In vitro* antibacterial activities of PAu@C/B. (a) Representative plate samples of *E. coli* and *S. aureus* after treatment with PAu@C/B or PAu@C/B + different laser irradiations, and (b) the corresponding quantitative analysis of *E. coli* and *S. aureus*. (c) SEM images of *E. coli* and *S. aureus* after being treated with PAu@C/B or PAu@C/B with different laser irradiations (scale bar: 1 μm). (d) Live/Dead staining of *E. coli and S. aureus* after treatment with PAu@C/B or PAu@C/B with different laser irradiations; live bacteria were stained green, and dead bacteria were stained red (scale bar: 20 μm). (*: $p < 0.05$; **: $p < 0.01$, ***: $p < 0.001$). (For interpretation of the references to color in this figure legend, the reader is referred to the web version of this article.)

and AuNPs [43] (Fig. 2a). It can be observed from Fig. 2b that by illuminating with 808 nm laser (1.5 W/cm^2) for 10 min, PAu and PAu@C/B possessed a similar prominent ability to increase their aqueous solutions from room temperature to 63.3 ℃ and 60.6 ℃, respectively. The photothermal conversion efficiencies of PAu and PAu@C/B enhanced to 57.7 % and 51.1 %, respectively (Fig. 2b, Fig. S5) [46]. This result is corelated to the broadening UV–vis absorption of PAu@C/B (Fig. 1e). In addition, the temperature profiles of PAu@C/B depend on the concentration and laser power density (Fig. S6), suggesting that we can maintain a mild temperature (~45 °C) on demand by controlling the laser power density. According to TEM results of PAu@C/B before and after NIR irradiation, it could be observed that the PAu@C/B size and solution color changed little with the increase in solution temperature (Fig. S7). This efficiency did not decrease obviously during the five laser on/off cycles (Fig. 2c), highlighting the excellent stability of PAu@C/B for the photothermal effect. The above results suggest that the excellent photothermal performance of PAu@C/B hybrid nanoflowers makes them appropriate for mild photothermal therapy.

3.2.2. *Photodynamic effect of PAu@C/B*

The photodynamic effect of PAu@C/B under 660 nm laser (1 W/cm^2) was then evaluated (Fig. 2d). We determined the singlet oxygen

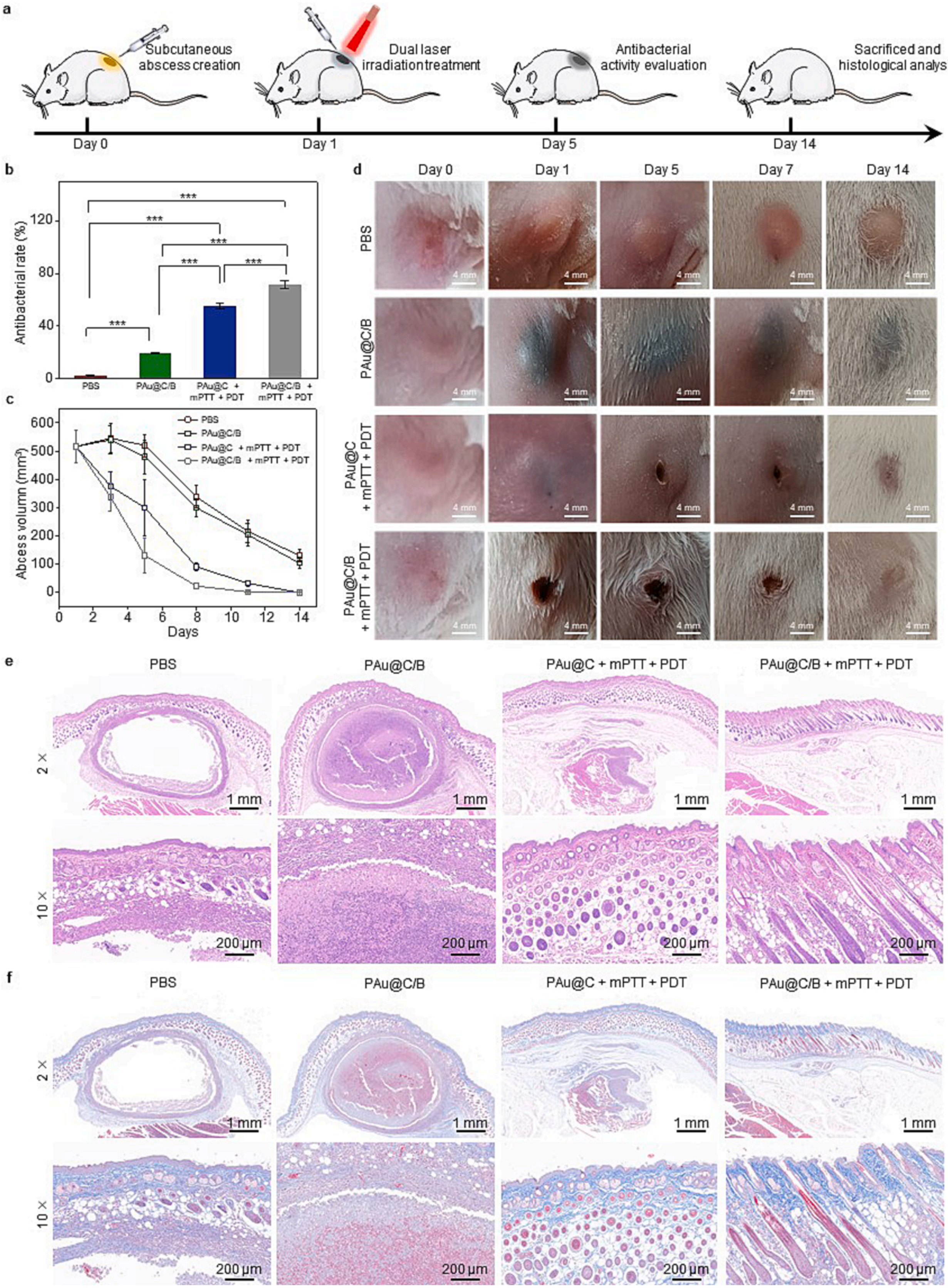

Fig. 4. The antimicrobial activity of PAu@C/B *in vivo* was examined in the subcutaneous abscess model. (a) Schematic diagram of PAu@C/B for the antibacterial therapeutic process *in vivo*. (b) Histogram of bacterial colonies obtained from the infected tissues of mice under 5 days of treatments. (c) Quantifying abscess areas in the infected mice treated with different materials for up to 14 days. (d) Changes in abscess in mice within 14 days. (e) H&E staining results of tissues harvested on day 14 (f) Masson staining results of tissues harvested on day 14.

($^1O_2$) level generated from PAu@C/B using 1,3-diphenylisobenzofuran (DPBF) as the fluorescent probe [47]. It can be observed that the PAu@C/B group exhibited an obviously and significantly decreased absorption of DPBF at 410 nm (Fig. 2e and f). For comparison, the AuNFs and PAu groups had no obvious absorption changes (Fig. S8). Furthermore, we measured the singlet oxygen ($^1O_2$) generation capacity by electron spin resonance (ESR) spectroscopy (Fig. S9). The results clearly demonstrated that the Ce6 released from PAu@C/B enable the $^1O_2$ generation. According to our findings, the superior synergistic mPTT and PDT effects of PAu@C/B demonstrated significant antibacterial potential.

3.2.3. Photo-triggered release of drugs from PAu@C/B

The photo-triggered drug-controlled release of PAu@C/B was examined. Fig. 2g shows that more than 67.2 % of Ce6 and 55.2 % of BS were released in a controlled manner after 3 cycles of mild-photothermal irradiation (1.5 W/cm^2, 10 min, 45 °C). In contrast, less than 19.0 % of Ce6 and 36.3 % of BS were released from PAu@C/B without laser irradiation (Fig. 2h and SPS:refid::fig2i). The NIR-induced drug release was further investigated by irradiating PAu@C/B once at a mild temperature (45 °C). The accumulative release rates of Ce6 and BS from PAu@C/B after 3 days of NIR stimulation were 79.5 % and 85.9 %, respectively, which were almost 1.4 and 1.2-fold higher compared to PAu@C/B without NIR stimulation (shown in Fig. S10). Therefore, dual drugs released from PAu@C/B can be conveniently turned “on” and “off” by mild-photothermal effect. The controlled release of dual drugs is ascribed to the remote heating generating through the photothermal conversion of PAu@C/B. In this manner, the heat radiated into the surroundings can increase the local temperature, enhance the drug diffusion coefficient, and accelerate the release of the drug molecules.

Taken together, PAu@C/B can intelligently release drugs under NIR-irradiation, allowing a regulated release of Ce6 and BS efficiently. Combined with the synergistic PTT and PDT effect, this chemotherapy potentially provides a precise photo-based strategy for infectious skin regeneration.

3.3. Biocompatibility evaluation and macrophage response to PAu@C/B nanoflowers in vitro

To evaluate the biocompatibility of AuNFs, PAu and PAu@C/B, cytotoxicity tests were performed on mammalian cells. The cell viability of PAu@C/B on fibroblasts (L929 cells) was evaluated using live-dead staining, and the results showed no obvious cell death in AuNFs, PAu, and PAu@C/B treatment groups (Fig. S11a). Even at high concentrations (50 μg/mL), the cell metabolism levels of PAu and PAu@C/B groups were higher than the PBS control, indicating the good biocompatibility of the hybrid nanoflowers (Fig. S11b).

To examine the effect of nanoflower carriers (PAu) on immune cell (macrophage) response, PAu at graded concentrations (0/10/50 μg/mL, 0 μg/mL served as the vehicle control) were used to treat RAW 264.7 cells (macrophage cell line) under the stimulation of 100 ng/mL lipopolysaccharides (LPS) to simulate the condition of infection associated inflammation. The mRNA levels (shown in Fig. S11c) of inflammatory/M1 markers (CD80, CD86, IL-1β, IL-6, and TNF) were down-regulated following PAu-treatment. On the other hand, the mRNA level of tissue regenerative/M2 marker CD206 was up-regulated by PAu in a dose-dependent manner, suggesting that PAu can potentially suppress the infection-associated inflammation and facilitate the M1-to-M2 conversion to benefit tissue healing. As a result, PAu should be the ideal carrier for anti-inflammatory drug delivery.

3.4. In vitro antibacterial activity of PAu@C/B hybrid nanoflowers

We evaluate the antibacterial activities of PAu@C/B against *S. aureus* and *E. coli* under 660 nm VIS, 808 nm NIR, and dual laser irradiation, because these hybrid nanoflowers possess high photothermal conversion efficiency and excellent singlet oxygen generation performance. As shown in Fig. 3a (and Fig. S12), the antibacterial effects of hybrid nanoflowers were not significant in the absence of laser irradiation. Under single laser irradiation, the bactericidal efficiencies of the PAu@C/B + PDT group were 27.0 % and 43.1 % for *E. coli* and *S. aureus*, respectively, and those of the PAu@C/B + mPTT group were 71.7 % and 76.1 %, respectively. These results indicate that the mild photothermal (45 ℃) or photodynamic treatment alone is insufficient for PAu@C/B to achieve a desirable antibacterial effect. On the other hand, mPTT showed a higher antibacterial efficiency compared to PDT. This result is consistent with the previous report [48,49]. Interestingly, under dual laser irradiation, the PAu@C/B exhibited significant antibacterial effects, as shown by the antibacterial rates over 98 % for both *S. aureus* and *E. coli*. This highly-efficient antibacterial performance contributes to the synergistic effects of mPTT and PDT (Fig. 3b). The membrane integrity of the treated bacteria was further investigated. As shown in Fig. 3c, E. *coli* (rod shape) and *S. aureus* (spherical shape) in PBS exhibited the typical morphologies with smooth surfaces. However, the PAu@C/B + mPTT, PAu@C/B + PDT, and PAu@C/B + mPTT + PDT treatments adversely affected the integrity of the bacterial cell membranes. It can be observed that the bacterial membranes of *E. coli* become distorted and wrinkled, while those of *S. aureus* showed apparent lesions and holes.

Live/dead staining of *E. coli and S. aureus* was performed to further examine the antibacterial ability of PAu@C/B with various NIR stimulation. Without laser irradiation, bacteria showed green fluorescence after treatment with PBS or PAu@C/B, indicating that the bacterial activity has not decreased. Furthermore, the PAu@C/B + PDT and PAu@C/B + mPTT groups presented a gradually increased yellow fluorescence (overlapping the red and green fluorescence). Notably, most stained bacteria exhibited red fluorescence, demonstrating that the highest antibacterial activity of PAu@C/B can be obtained through dual-NIR stimulation to trigger the mPTT and PDT effects. These findings are consistent with the results of the conventional plate assay.

It is well known that the bacterial biofilm will shield bacteria from antibiotics, which is one of the most decisive factors in developing drug resistance [46]. Therefore, adhered biofilms were stained with crystal violet (CV) and subsequently quantified to evaluate the effect of PAu@C/B on the eradication of biofilms in response to various NIR stimulation. The biofilm in the PBS group is relatively intact (Fig. S13a and b), whereas that in the PAu@C/B + mPTT + PDT group reduces by almost 90 %. The findings suggest that our PAu@C/B with dual laser irradiation is able to eliminate drug-resistant bacteria through mPTT and PDT. These results indicate that our antibacterial strategy based on the synergistic effects of mPTT and PDT is significantly superior to mPTT or PDT alone. The combination of mPTT and PDT can effectively eliminate both gram-positive and gram-negative bacteria, as well as the biofilm. This synergistic antibacterial mechanism may be attributed to the reason that a mild photothermal treatment at 45 °C (which shall avoid the damage on healthy tissue) could increase the permeability of the bacterial membrane, thereby facilitating the entry of singlet oxygen ($^1O_2$) into the bacteria and causing more severe bacterial death via the inactivation of enzymes, disruption of metabolic signaling, and denaturation of protein structures.

3.5. PAu@C/B antibacterial and anti-inflammatory effects in vivo

To verify the antimicrobial and immunomodulatory activities of PAu@C/B *in vivo*, the PAu@C and PAu@C/B are used to treat the mice model of subcutaneous abscess infected with *MRSA* and then irradiated by dual laser irradiation (808 nm, 45℃, 10 min; 660 nm, 300 mW, 10 min) as shown in Fig. 4a. The temperature of the PAu@C and PAu@C/B groups considerably increased after NIR irradiation from 0 to 1 min and stayed around 45 °C for the following 10 min (Fig. S14a,b). The bactericidal effect is evaluated by analyzing the bacterial colonies harvested from the *in vivo* subcutaneous abscesses obtained on day 5. Notably, PAu@C/B shows negligible antimicrobial effect compared to the control

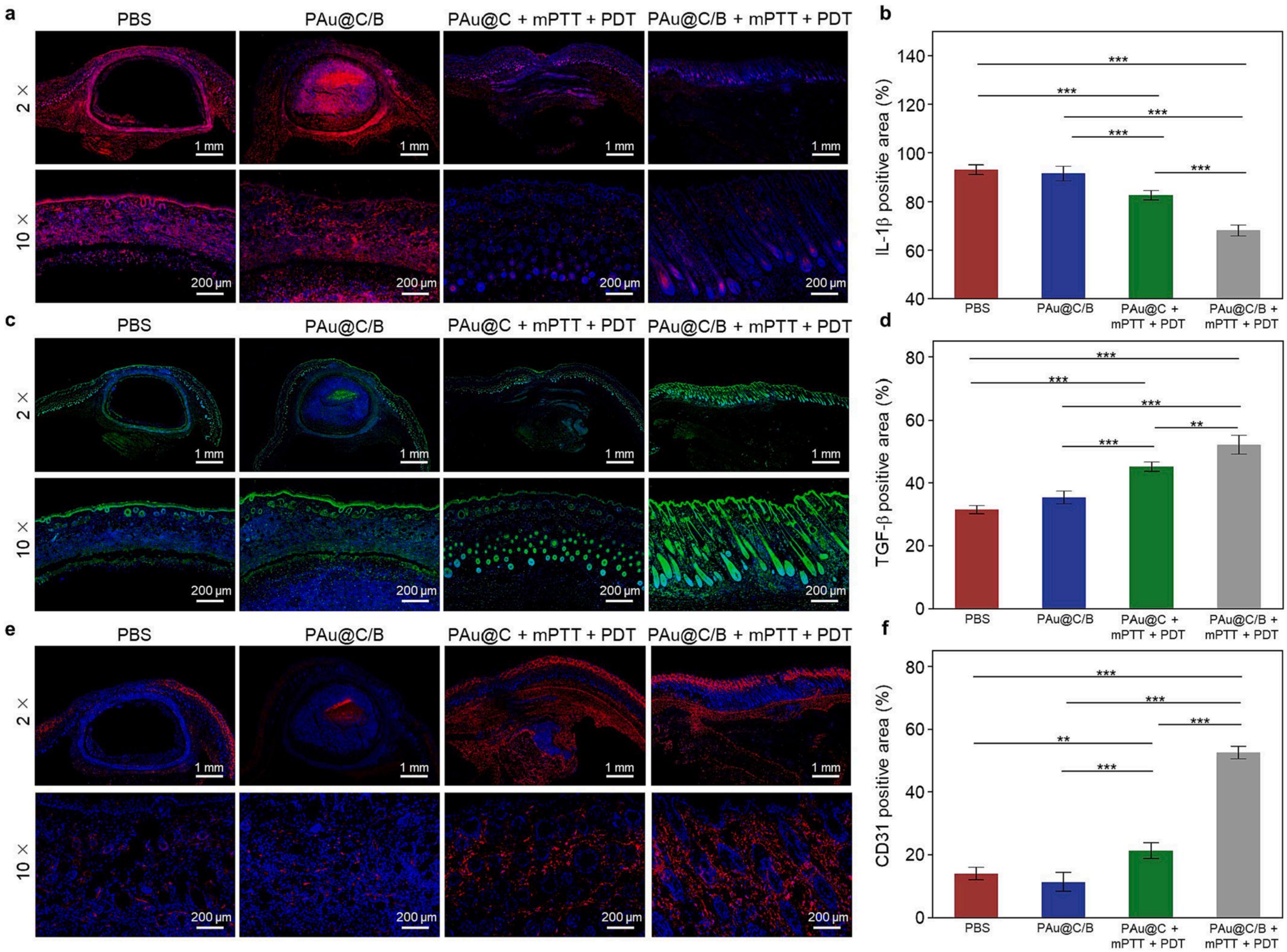

Fig. 5. Immunofluorescence staining of (a&b) IL-1β, (c&d) TGF-β and (e&f) CD31 in subcutaneous abscess model treated with PAu@C/B (day 14) *in vivo*.

without laser irradiation. Under dual laser irradiation, however, the number of colonies in the PAu@C and PAu@C/B groups decreases to 45.3 % and 28.3 %, respectively, indicating that the synergistic mPTT and PDT enhanced the bactericidal effect *in vivo* (Fig. 4b; Fig. S14c).

After 14 days of therapy, abscesses could be observed in the PBS and PAu@C/B groups, indicating that the limited antibacterial effects of these two groups would delay tissue reconstruction (Fig. 4c and d). In contrast, under dual laser irradiation, both PAu@C and PAu@C/B achieved relatively good therapeutic effects, as evidenced by the histological observation that the infected sites were scabbed and nearly healed (Fig. 4c and d). The body weight of the mice remains stable during therapies, and no significant differences could be found within the four groups (Fig. S14d).

To further evaluate the tissue infection, the histological analysis of abscess sections (harvested on day 7 and day 14) was performed by the H&E staining (Fig. 4e and Fig. S15). Consistent with the digital photographs on day 7 and 14, H&E staining results demonstrated that the abscesses area became smaller after the synergistic effect of mPTT and PTT (both in PAu@C + mPTT + PDT and PAu@C/B + mPTT + PDT groups). Furthermore, the thickness of granulation tissue in the PAu@C/B + mPTT + PDT group was significantly increased, and the formation of hair follicle structures was observed in day 14 samples. In addition, a large amount of collagen deposition was observed in the PAu@C/B + mPTT + PDT treatment group, indicating the healing and maturation of tissues (Fig. 4f). These results demonstrated the synergistic effects of mild photothermal (mPTT) and photodynamic (PDT) for rapid bacterial elimination *in vivo* (Fig. 4b,c,d).

Bacteria infection along with the mild photothermal and photodynamic side-effects can trigger and prolong an inflammatory response in the tissue, which is detrimental to tissue repair. The effects of the PAu@C/B system on inflammatory cytokine/tissue regenerative growth factor release were evaluated through the label of IL-1β (inflammatory cytokine [50]) and TGF-β (tissue-regenerative factor [51]). Owing to the controlled-release of anti-inflammatory drug, the IL-1β production (Fig. 5a,b; Fig. S16) in the PAu@C/B + mPTT + PDT group significantly decreased compared to the PAu@C + mPTT + PDT group. Meanwhile, the TGF-β expression was upregulated following PAu@C/B + mPTT + PDT treatment (Fig. 5c,d; Fig. S17) compared with other groups. Accordingly, the expression of inflammatory immune cell (e.g., M1 macrophage) marker iNOS was downregulated in the PAu@C/B + mPTT + PDT group, while the expression of anti-inflammatory immune cell (e.g., M2 macrophage) marker arginase was significantly upregulated, compared with other groups (Fig. S18). These results suggest that the PAu@C/B system effectively suppress inflammation during infectious wound-healing, owing to its capacity to release anti-inflammatory BS. This can modulate the unfavorable microenvironment owing to mPTT and PDT to benefit tissue regeneration. Additionally, as shown in Fig. 5e, f and Fig. S19, the PAu@C/B + mPTT + PDT group was found to promote local angiogenesis (CD31-positive area, a neovascularization marker expressed in newly formed blood vessels in the lesions [52]), thereby further contributing to wound-healing. Therefore, the hybrid nanoflowers serve as a viable tool to achieve both the photodynamic

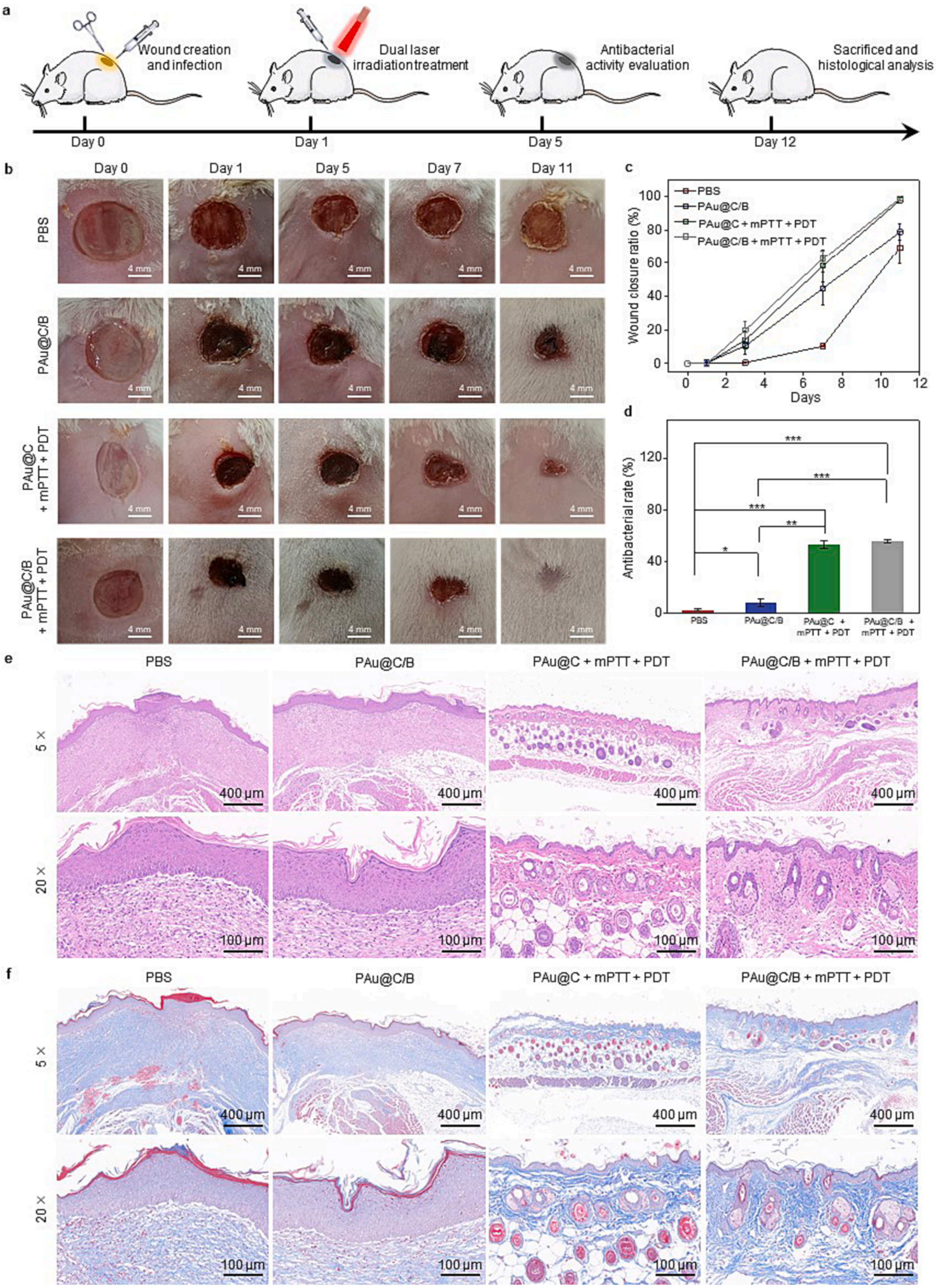

Fig. 6. The effect of PAu@C/B in infectious wound-healing *in vivo*. (a) Schematic diagram of the therapeutic process of PAu@C/B *in vivo*. (b) Photos showing the wound-healing processes in different treatment groups. (c) Wound-healing rates for different treatment groups on day 0, day 1, day 5, day 7, and 12. (d) Histogram of bacterial colonies obtained from infected tissues of mice with different treatments on day 5. (e) H&E staining of skin wound tissues on day 12. (f) Masson staining of skin wound tissues on day 12.

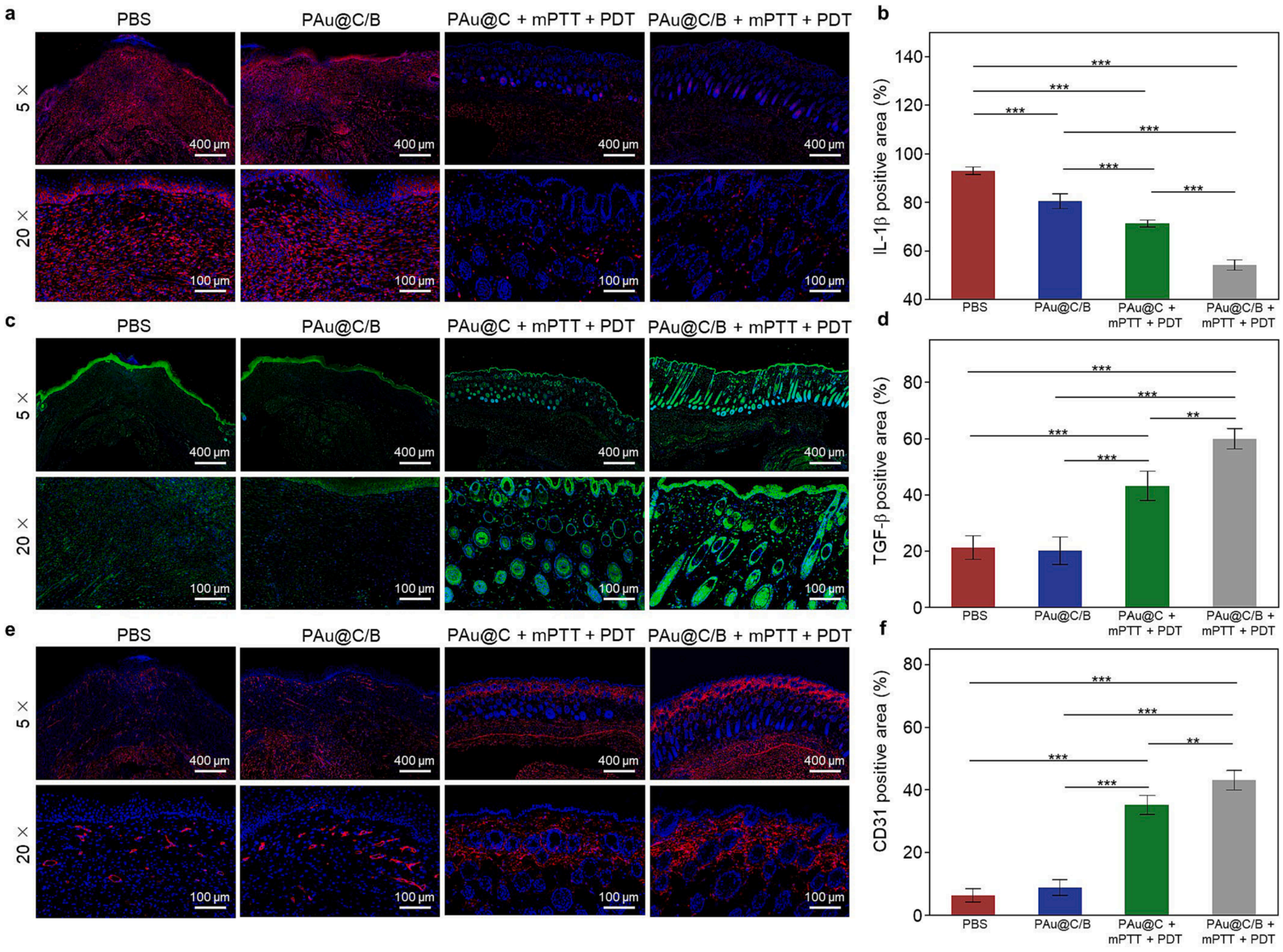

Fig. 7. Representative images of (a&b) IL-1β, (c&d) TGF-β and (e&f) CD31 expression on day 12 (detected by immunofluorescence staining).

assisted mPTT and PDT for effective bacterial infection control, along with the controlled release of anti-inflammatory drugs to improve the microenvironment for tissue regeneration. Based on the excellent antibacterial and anti-inflammatory activity of the hybrid nanoflowers, PAu@C/B + mPTT + PDT can eradicate most bacteria without causing severe inflammation, thereby promoting the regeneration of infected tissue.

3.6. The therapeutical effects of PAu@C/B in infectious wound-healing

A mouse skin wound model with *MRSA* infection was created to further investigate the effect of PAu@C/B with NIR in infectious wound-healing. In the PAu@C + mPTT + PDT and PAu@C/B + mPTT + PDT groups, the photothermal temperatures were monitored and dynamically adjusted to 45 °C for 10 min of irradiation (Fig. S20a,b), then illuminated with a 660 nm laser for 10 min (300 mW). After 12 days of treatment, the quantification of the wound area is determined by the results of the macroscopic photographs (Fig. 6b). The results showed that mice treated with mPTT + PDT exhibited significantly faster wound closure than the other groups, with nearly 60 % closure achieved on day 7 and complete healing by day 12 (Fig. 6c). Furthermore, consistent with the results shown in Fig. 4d and Fig. S14c, the results in Fig. 6d and Fig. S20c further suggest the superior antibacterial performance of PAu@C/B and PAu@C under dual laser irradiation.

Subsequently, we conducted a histological analysis of the wound tissues. On day 7, the PAu@C/B + mPTT + PDT nm group showed normal healing as indicated by H&E staining (Fig. S21). In contrast, other groups (especially the PBS and PAu@C/B groups) showed obvious inflammatory cell infiltration and accumulation at the wound areas. Accordingly, on day 12, H&E staining results showed a large number of necrotic cells in the infected areas of the PBS and PAu@C/B groups, while the epidermis of the PAu@C + mPTT + PDT and PAu@C/B + mPTT + PDT groups showed new blood vessels and fibroblast-like cells (Fig. 6e). Furthermore, well-organized stratified epithelial layer and hair follicle-like tissues were found in the PAu@C/B + mPTT + PDT group. Masson staining was used to determine collagen deposition in the wound, and the results (Fig. 6f) demonstrated that the wounds treated with PAu@C/B + mPTT + PDT had a denser accumulation of collagen fibers with a parallel arrangement. These results suggest that PAu@C/B with dual laser irradiation can significantly promote infectious wound-healing and tissue maturation.

Immunohistology was used to evaluate wound tissue inflammation. Similar to the results obtained from the subcutaneous abscess mode, as shown in Fig. 7a,b, PAu@C/B with dual laser irradiation significantly reduced IL-1β expression (Fig. S22) while induced TGF-β production and distribution (Fig. 7c,d; Fig. S23). The expression of inflammatory immune cell (e.g., M1 macrophage) maker iNOS was downregulated by PAu@C/B + mPTT + PDT, and the expression of anti-inflammatory immune cell (e.g., M2 macrophage) arginase was upregulated, suggesting that the treatment of PAu@C/B with dual laser irradiation can facilitate the M1-to-M2 macrophage phenotype switch in *in vivo* wound-healing (Fig. S24). Furthermore, the upregulated CD31 indicates that

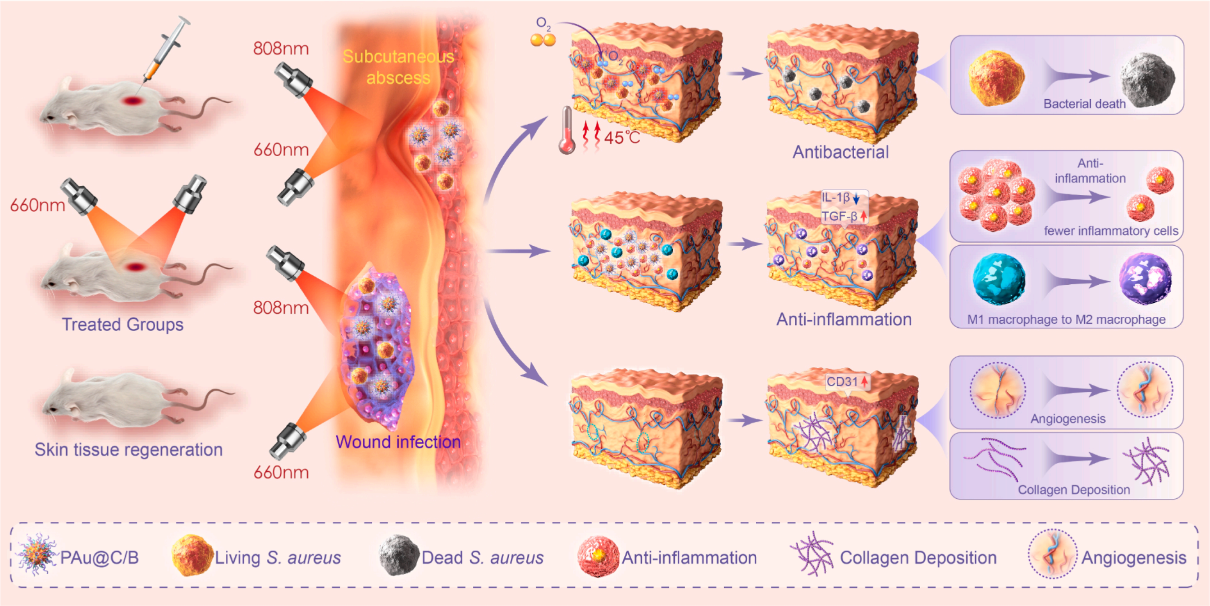

Fig. 8. Schematic of the mechanisms of PAu@C/B under dual laser radiation for accelerating infectious skin wound-healing.

PAu@C/B with dual laser irradiation can improve angiogenesis (Fig. 7e, f and Fig. S25). Our findings, therefore, demonstrated that PAu@C/B could efficiently improve the infectious wound-healing in the mechanisms of mPTT-PDT-directed bacterial control and immunomodulation achieved through the controlled drug (BS) delivery.

Additionally, the biosafety of the PAu@C/B system, an unneglectable index in the biomedical application of nanomaterials, was evaluated by monitoring the bodyweight change during treatment and histological observation of major organs obtained from the mice skin wound model. The body weight of the mice remained stable after various treatments, and no significant difference could be found between the four groups (Fig. S20d). H&E staining results demonstrated that the PAu@C/B + mPTT + PDT group did not cause significant histological changes in the major organs of mice (Fig. S26) compared to the PBS group. Therefore, these results suggest that PAu@C/B with dual laser irradiation (660 nm + 808 nm) is biocompatible *in vivo*.

These findings provide further evidence that the PDT assisted mPTT can effectively control infection. The photothermal performance of the hybrid nanoflowers can also trigger a controlled release of anti-inflammatory drug, which modulates the local microenvironment to promote tissue regeneration, thereby accelerating collagen deposition and angiogenesis, improving skin tissue regeneration (Fig. 8).

4. Conclusion

This study developed a multifunctional nano-system with NIR-triggered mild-temperature photothermal, photodynamic, and controlled drug delivery performances. The developed hybrid nanoflowers (PAu@C/B) with dual drug loading facilitated bacterial clearance via inducing mPTT and PDT, and anti-inflammation via controlled drug delivery, which synergistically and effectively promoted the infectious skin tissue regeneration. The mild photothermal performance (45 °C) combined with the photodynamic effect not only achieved the highest antibacterial efficiency, but also minimized hyperthermia-induced adverse effects on healthy tissue. In addition, the controlled photo-triggered drug (BS) release could effectively modulate the inflammatory microenvironment to favor endogenous growth factor release, collagen deposition, and accelerating vascularization. In summary, the multifunctional hybrid nanoflowers with dual laser irradiation can substantially enhance wound-healing and tissue regeneration *in vivo*. Our study, therefore, provides an advanced drug-delivery nanomaterial and a potential mild photothermal therapeutical system for infectious tissue regeneration in the future.

CRediT authorship contribution statement

Jixuan Hong: Writing – review & editing, Writing – original draft, Visualization, Validation, Methodology, Investigation, Data curation. **Jiaqi Zhu:** Visualization, Methodology, Investigation, Data curation. **Xiaxin Cao:** Investigation. **Boqi Pang:** Investigation. **Jiaru Xian:** Investigation. **Xueqiong Yin:** Investigation, Funding acquisition. **Qiaoyuan Deng:** Writing – review & editing, Supervision, Investigation, Funding acquisition. **Maohua Chen:** Investigation, Funding acquisition. **Ziyu Qin:** Investigation. **Chaozong Liu:** Investigation, Funding acquisition. **Swastina Nath Varma:** . **Yin Xiao:** Investigation. **Lan Xiao:** Writing – review & editing, Supervision, Methodology, Investigation, Funding acquisition, Conceptualization. **Mengting Li:** Writing – review & editing, Supervision, Project administration, Methodology, Investigation, Funding acquisition, Conceptualization.

Declaration of competing interest

The authors declare that they have no known competing financial interests or personal relationships that could have appeared to influence the work reported in this paper.

Data availability

Data will be made available on request.

Acknowledgements

This work was supported by the Hainan Provincial Natural Science Foundation of China (No. 520QN225, 520QN224); National Natural Science Foundation of China (No. 32360238); Natural Science Foundation of Hainan Province (No. GHYF2022001); Key Scientific and Technological Project of Haikou City (2021024). Engineering; Physical Sciences Research Council via DTP CASE Program (grant No. EP/T517793/1); and Young Researcher Grant (19-066) from the Osteology Foundation, Switzerland.

Appendix A. Supplementary data

Supplementary data to this article can be found online at https://doi.org/10.1016/j.cej.2024.148937.

References

[1] J. Min, K.Y. Choi, E.C. Dreaden, R.F. Padera, R.D. Braatz, M. Spector, P. T. Hammond, Designer dual therapy nanolayered implant coatings eradicate biofilms and accelerate bone tissue repair, ACS Nano 10 (4) (2016) 4441–4450, https://doi.org/10.1021/acsnano.6b00087.

[2] K.A. Brogden, Antimicrobial peptides: pore formers or metabolic inhibitors in bacteria? Nat. Rev. Microbiol. 3 (3) (2005) 238–250, https://doi.org/10.1038/nrmicro1098.

[3] P. Li, Y.F. Poon, W. Li, H.-Y. Zhu, S.H. Yeap, Y. Cao, X. Qi, C. Zhou, M. Lamrani, R. W. Beuerman, A polycationic antimicrobial and biocompatible hydrogel with microbe membrane suctioning ability, Nat. Mater. 10 (2) (2011) 149–156.

[4] D.G. Metcalf, P.G. Bowler, Clinical impact of an anti-biofilm Hydrofiber dressing in hard-to-heal wounds previously managed with traditional antimicrobial products and systemic antibiotics, Burns & Trauma 8 (2020), https://doi.org/10.1093/burnst/tkaa004.

[5] J. He, M. Shi, Y. Liang, B. Guo, Conductive adhesive self-healing nanocomposite hydrogel wound dressing for photothermal therapy of infected full-thickness skin wounds, Chem. Eng. J. 394 (2020) 124888, https://doi.org/10.1016/j.cej.2020.124888.

[6] X. Zhao, D. Pei, Y. Yang, K. Xu, J. Yu, Y. Zhang, Q. Zhang, G. He, Y. Zhang, A. Li, Y. Cheng, X. Chen, Green tea derivative driven smart hydrogels with desired functions for chronic diabetic wound treatment, Adv. Funct. Mater. 31 (18) (2021) 2009442, https://doi.org/10.1002/adfm.202009442.

[7] S. Zhu, Q. Dai, L. Yao, Z. Wang, Z. He, M. Li, H. Wang, Q. Li, H. Gao, X. Cao, Engineered multifunctional nanocomposite hydrogel dressing to promote vascularization and anti-inflammation by sustained releasing of Mg2+ for diabetic wounds, Compos. B Eng. 231 (2022) 109569, https://doi.org/10.1016/j.compositesb.2021.109569.

[8] J. Davies, Inactivation of antibiotics and the dissemination of resistance genes, Sci. 264 (5157) (1994) 375–382, https://doi.org/10.1126/science.8153624.

[9] P.V. AshaRani, G. Low Kah Mun, M.P. Hande, S. Valiyaveettil, Cytotoxicity and genotoxicity of silver nanoparticles in human cells, ACS Nano 3 (2) (2009) 279–290, https://doi.org/10.1021/nn800596w.

[10] S.R. Modi, H.H. Lee, C.S. Spina, J.J. Collins, Antibiotic treatment expands the resistance reservoir and ecological network of the phage metagenome, Nat. 499 (7457) (2013) 219–222, https://doi.org/10.1038/nature12212.

[11] J. Zhu, J. Tian, C. Yang, J. Chen, L. Wu, M. Fan, X. Cai, L-Arg-Rich amphiphilic dendritic peptide as a versatile no donor for NO/photodynamic synergistic treatment of bacterial infections and promoting wound healing, Small 17 (32) (2021) 2101495, https://doi.org/10.1002/smll.202101495.

[12] K. Yang, S. Zhao, B. Li, B. Wang, M. Lan, X. Song, Low temperature photothermal therapy: advances and perspectives, Coord. Chem. Rev. 454 (2022) 214330, https://doi.org/10.1016/j.ccr.2021.214330.

[13] J. Qiu, M. Xie, T. Wu, D. Qin, Y. Xia, Gold nanocages for effective photothermal conversion and related applications, Chem. Sci. 11 (48) (2020) 12955–12973, https://doi.org/10.1039/d0sc05146b.

[14] K. Ma, Y. Li, Z. Wang, Y. Chen, X. Zhang, C. Chen, H. Yu, J. Huang, Z. Yang, X. Wang, Z. Wang, Core-shell gold nanorod@layered double hydroxide nanomaterial with highly efficient photothermal conversion and its application in antibacterial and tumor therapy, ACS Appl. Mater. Interfaces 11 (33) (2019) 29630–29640, https://doi.org/10.1021/acsami.9b10373.

[15] C. Li, J. Xian, J. Hong, X. Cao, C. Zhang, Q. Deng, Z. Qin, M. Chen, X. Zheng, M. Li, J. Hou, Y. Zhou, X. Yin, Dual photothermal nanocomposites for drug-resistant infectious wound management, Nanoscale 14 (31) (2022) 11284–11297, https://doi.org/10.1039/d2nr01998a.

[16] M. Zhang, H. Zhang, J. Feng, Y. Zhou, B. Wang, Synergistic chemotherapy, physiotherapy and photothermal therapy against bacterial and biofilms infections through construction of chiral glutamic acid functionalized gold nanobipyramids, Chem. Eng. J. 393 (2020) 124778, https://doi.org/10.1016/j.cej.2020.124778.

[17] C. Cao, N. Yang, Y. Zhao, D. Yang, Y. Hu, D. Yang, X. Song, W. Wang, X. Dong, Biodegradable hydrogel with thermo-response and hemostatic effect for photothermal enhanced anti-infective therapy, Nano Today 39 (2021) 101165, https://doi.org/10.1016/j.nantod.2021.101165.

[18] Z. Xu, Y. Gao, S. Meng, B. Yang, L. Pang, C. Wang, T. Liu, Mechanism and in vivo evaluation: photodynamic antibacterial chemotherapy of lysine-porphyrin conjugate, Front. Microbiol. 7 (2016).

[19] C. Mao, Y. Xiang, X. Liu, Y. Zheng, K.W.K. Yeung, Z. Cui, X. Yang, Z. Li, Y. Liang, S. Zhu, S. Wu, Local photothermal/photodynamic synergistic therapy by disrupting bacterial membrane to accelerate reactive oxygen species permeation and protein leakage, ACS Appl. Mater. Interfaces 11 (19) (2019) 17902–17914, https://doi.org/10.1021/acsami.9b05787.

[20] K. Zhou, X. Qiu, L. Xu, G. Li, B. Rao, B. Guo, D. Pei, A. Li, G. He, Poly (selenoviologen)-assembled upconversion nanoparticles for low-power single-NIR light-triggered synergistic photodynamic and photothermal antibacterial therapy, ACS Appl. Mater. Interfaces 12 (23) (2020) 26432–26443, https://doi.org/10.1021/acsami.0c04506.

[21] R. Peng, Y. Luo, Q. Cui, J. Wang, L. Li, Near-infrared conjugated oligomer for effective killing of bacterial through combination of photodynamic and photothermal treatment, ACS Applied Bio Materials 3 (2) (2020) 1305–1311, https://doi.org/10.1021/acsabm.9b01242.

[22] Q. Cui, H. Yuan, X. Bao, G. Ma, M. Wu, C. Xing, Synergistic photodynamic and photothermal antibacterial therapy based on a conjugated polymer nanoparticle-doped hydrogel, ACS Applied Bio Materials 3 (7) (2020) 4436–4443, https://doi.org/10.1021/acsabm.0c00423.

[23] J. Larouche, S. Sheoran, K. Maruyama, M.M. Martino, Immune Regulation of skin wound healing: mechanisms and novel therapeutic targets, Adv. Wound Care 7 (7) (2018) 209–231, https://doi.org/10.1089/wound.2017.0761.

[24] T.A. Wilgus, Immune cells in the healing skin wound: Influential players at each stage of repair, Pharmacol. Res. 58 (2) (2008) 112–116, https://doi.org/10.1016/j.phrs.2008.07.009.

[25] A.R. Armiento, L.P. Hatt, G. Sanchez Rosenberg, K. Thompson, M.J. Stoddart, Functional biomaterials for bone regeneration: a lesson in complex biology, Adv. Funct. Mater. 30 (44) (2020) 1909874, https://doi.org/10.1002/adfm.201909874.

[26] P. Krzyszczyk, R. Schloss, A. Palmer, F. Berthiaume, The role of macrophages in acute and chronic wound healing and interventions to promote pro-wound healing phenotypes, Front. Physiol. 9 (2018).

[27] M. Hesketh, K.B. Sahin, Z.E. West, R.Z. Murray, Macrophage phenotypes regulate scar formation and chronic wound healing, Int. J. Mol. Sci. 18 (7) (2017) 1545.

[28] J.-E. Won, Y.S. Lee, J.-H. Park, J.-H. Lee, Y.S. Shin, C.-H. Kim, J.C. Knowles, H.-W. Kim, Hierarchical microchanneled scaffolds modulate multiple tissue-regenerative processes of immune-responses, angiogenesis, and stem cell homing, Biomaterials 227 (2020) 119548, https://doi.org/10.1016/j.biomaterials.2019.119548.

[29] L. Xiao, F. Wei, Y. Zhou, G.J. Anderson, D.M. Frazer, Y.C. Lim, T. Liu, Y. Xiao, Dihydrolipoic acid-gold nanoclusters regulate microglial polarization and have the potential to alter neurogenesis, Nano Lett. 20 (1) (2020) 478–495, https://doi.org/10.1021/acs.nanolett.9b04216.

[30] R. Toita, J.-H. Kang, A. Tsuchiya, Phosphatidylserine liposome multilayers mediate the M1-to-M2 macrophage polarization to enhance bone tissue regeneration, Acta Biomater. 154 (2022) 583–596, https://doi.org/10.1016/j.actbio.2022.10.024.

[31] A.B. da Silva, K.B. Rufato, A.C. de Oliveira, P.R. Souza, E.P. da Silva, E.C. Muniz, B. H. Vilsinski, A.F. Martins, Composite materials based on chitosan/gold nanoparticles: from synthesis to biomedical applications, Int. J. Biol. Macromol. 161 (2020) 977–998, https://doi.org/10.1016/j.ijbiomac.2020.06.113.

[32] B.N. Khlebtsov, A.M. Burov, N.G. Khlebtsov, Polydopamine coating decreases longitudinal plasmon of Au nanorods: Experiment and simulations, Appl. Mater. Today 15 (2019) 67–76, https://doi.org/10.1016/j.apmt.2018.12.017.

[33] N.L. Rosi, D.A. Giljohann, C.S. Thaxton, A.K.R. Lytton-Jean, M.S. Han, C.A. Mirkin, Oligonucleotide-modified gold nanoparticles for intracellular gene regulation, Sci. 312 (5776) (2006) 1027–1030, https://doi.org/10.1126/science.1125559.

[34] D.T. Wiley, P. Webster, A. Gale, M.E. Davis, Transcytosis and brain uptake of transferrin-containing nanoparticles by tuning avidity to transferrin receptor, Proc. Natl. Acad. Sci. 110 (21) (2013) 8662–8667, https://doi.org/10.1073/pnas.1307152110.

[35] P. Ghosh, G. Han, M. De, C.K. Kim, V.M. Rotello, Gold nanoparticles in delivery applications, Adv. Drug Deliv. Rev. 60 (11) (2008) 1307–1315, https://doi.org/10.1016/j.addr.2008.03.016.

[36] M. Tebbe, C. Kuttner, M. Männel, A. Fery, M. Chanana, Colloidally Stable and surfactant-free protein-coated gold nanorods in biological media, ACS Appl. Mater. Interfaces 7 (10) (2015) 5984–5991, https://doi.org/10.1021/acsami.5b00335.

[37] G. Cao, F. Xu, S. Wang, K. Xu, X. Hou, P. Wu, Gold nanoparticle-based colorimetric assay for selenium detection via hydride generation, Anal. Chem. 89 (8) (2017) 4695–4700, https://doi.org/10.1021/acs.analchem.7b00337.

[38] X. Huang, S. Tang, X. Mu, Y. Dai, G. Chen, Z. Zhou, F. Ruan, Z. Yang, N. Zheng, Freestanding palladium nanosheets with plasmonic and catalytic properties, Nat. Nanotechnol. 6 (1) (2011) 28–32, https://doi.org/10.1038/nnano.2010.235.

[39] J. Hong, M. Chen, J. Xian, C. Li, X. Zheng, Q. Deng, X. Yin, M. Li, Preparation of Au-based hybrid nanoflowers as efficient photothermal agents for antibacterial application, Mater. Lett. 317 (2022), https://doi.org/10.1016/j.matlet.2022.132034.

[40] L. Yang, L. Xiao, W. Gao, X. Huang, F. Wei, Q. Zhang, Y. Xiao, Macrophages at low-inflammatory status improved osteogenesis via autophagy regulation, Tissue Eng. A (2021), https://doi.org/10.1089/ten.tea.2021.0015.

[41] A.L. Bookout, D.J. Mangelsdorf, Quantitative real-time PCR protocol for analysis of nuclear receptor signaling pathways, Nucl. Recept. Signal. 1 (1) (2003) nrs.01012, https://doi.org/10.1621/nrs.01012.

[42] S.A. Bustin, V. Benes, J.A. Garson, J. Hellemans, J. Huggett, M. Kubista, R. Mueller, T. Nolan, M.W. Pfaffl, G.L. Shipley, J. Vandesompele, C.T. Wittwer, The MIQE Guidelines: Minimum Information for Publication of Quantitative Real-Time PCR Experiments, Clin. Chem. 55 (4) (2009) 611–622, https://doi.org/10.1373/clinchem.2008.112797.

[43] J. Hong, M. Chen, J. Xian, C. Li, X. Zheng, Q. Deng, X. Yin, M. Li, Preparation of Au-based hybrid nanoflowers as efficient photothermal agents for antibacterial application, Mater. Lett. 317 (2022) 132034, https://doi.org/10.1016/j.matlet.2022.132034.

[44] Y. Wang, Y. Zhao, J. Wu, M. Li, J. Tan, W. Fu, H. Tang, P. Zhang, Negatively Charged Sulfur Quantum Dots for Treatment of Drug-Resistant Pathogenic Bacterial Infections, Nano Lett. 21 (22) (2021) 9433–9441, https://doi.org/10.1021/acs.nanolett.1c02697.

[45] S. Zhao, Y. Li, Q. Liu, S. Li, Y. Cheng, C. Cheng, Z. Sun, Y. Du, C.J. Butch, H. Wei, An Orally Administered CeO2@Montmorillonite nanozyme targets inflammation for inflammatory bowel disease therapy, Adv. Funct. Mater. 30 (45) (2020) 2004692, https://doi.org/10.1002/adfm.202004692.

[46] L. Zhang, S. Chen, R. Ma, L. Zhu, T. Yan, G. Alimu, Z. Du, N. Alifu, X. Zhang, NIR-Excitable PEG-Modified Au Nanorods for Photothermal Therapy of Cervical Cancer, ACS Applied Nano Materials 4 (12) (2021) 13060–13070, https://doi.org/10.1021/acsanm.1c02594.

[47] W. Zhang, B. Li, H. Ma, L. Zhang, Y. Guan, Y. Zhang, X. Zhang, P. Jing, S. Yue, Combining Ruthenium(II) Complexes with Metal-Organic Frameworks to Realize Effective Two-Photon Absorption for Singlet Oxygen Generation, ACS Appl. Mater. Interfaces 8 (33) (2016) 21465–21471, https://doi.org/10.1021/acsami.6b05817.

[48] Y. Zheng, Y. Zhu, J. Dai, J. Lei, J. You, N. Chen, L. Wang, M. Luo, J. Wu, Atomically precise Au nanocluster-embedded carrageenan for single near-infrared light-triggered photothermal and photodynamic antibacterial therapy, Int. J. Biol. Macromol. 230 (2023) 123452, https://doi.org/10.1016/j.ijbiomac.2023.123452.

[49] Y. Xie, W. Zheng, X. Jiang, Near-Infrared Light-Activated Phototherapy by Gold Nanoclusters for Dispersing Biofilms, ACS Appl. Mater. Interfaces 12 (8) (2020) 9041–9049, https://doi.org/10.1021/acsami.9b21777.

[50] X.-H. Qin, B. Senturk, J. Valentin, V. Malheiro, G. Fortunato, Q. Ren, M. Rottmar, K. Maniura-Weber, Cell-Membrane-Inspired Silicone Interfaces that Mitigate Proinflammatory Macrophage Activation and Bacterial Adhesion, Langmuir 35 (5) (2019) 1882–1894, https://doi.org/10.1021/acs.langmuir.8b02292.

[51] X. He, L. Dai, L. Ye, X. Sun, O. Enoch, R. Hu, X. Zan, F. Lin, J. Shen, A Vehicle-Free Antimicrobial Polymer Hybrid Gold Nanoparticle as Synergistically Therapeutic Platforms for Staphylococcus aureus Infected Wound Healing, Adv. Sci. 9 (14) (2022) 2105223, https://doi.org/10.1002/advs.202105223.

[52] Y. Liang, M. Li, Y. Yang, L. Qiao, H. Xu, B. Guo, pH/Glucose dual responsive metformin release hydrogel dressings with adhesion and self-healing via dual-dynamic bonding for athletic diabetic foot wound healing, ACS Nano 16 (2) (2022) 3194–3207, https://doi.org/10.1021/acsnano.1c11040.